AGU ADVANCING EARTH AND SPACE SCIENCES

JGR Atmospheres

Key Points:

- High-resolution CO_2 dynamic emission inventory greatly improves CO_2 simulations compared with Open-source Data Inventory for Anthropogenic CO_2 and Emission Database for Global Atmospheric Research
- Anthropogenic emission reductions cause CO_2 concentrations decrease by 4.6 (3.1) ppmv in Shanghai (Yangtze River Delta) during the COVID-19 pandemic
- Industrial and transportation emissions mainly dominate the reduction in CO_2 concentrations at the near surface and vertical altitude

Author Contributions:

Conceptualization: Yanyu Wang, Cheng Huang
Data curation: Chong Wei, Rusha Yan, Yusen Duan, Qizhen Liu, Wei Wang, Qianli Ma, Qianshan He
Formal analysis: Yanyu Wang, Xiao-Ming Hu, Wenling Liao, Tiantao Cheng
Funding acquisition: Cheng Huang, Chong Wei
Investigation: Hongli Wang
Methodology: Yanyu Wang, Xiao-Ming Hu, Jingyu An, Rusha Yan, Junjie Tian
Supervision: Cheng Huang, Renhe Zhang

Quantifying the Impact of COVID-19 Pandemic on the Spatiotemporal Changes of CO₂ Concentrations in the Yangtze River Delta, China

Yanyu Wang[1,2] ![ORCID], Cheng Huang[1] ![ORCID], Xiao-Ming Hu[3] ![ORCID], Chong Wei[1,4] ![ORCID], Jingyu An[1], Rusha Yan[1] ![ORCID], Wenling Liao[1], Junjie Tian[1], Hongli Wang[1] ![ORCID], Yusen Duan[5], Qizhen Liu[5], Wei Wang[6], Qianli Ma[7], Qianshan He[8,9] ![ORCID], Tiantao Cheng[2,10,11] ![ORCID], Hang Su[1,12] ![ORCID], and Renhe Zhang[2] ![ORCID]

[1]State Environmental Protection Key Laboratory of Formation and Prevention of Urban Air Pollution Complex, Shanghai Academy of Environmental Sciences, Shanghai, China, [2]Department of Atmospheric and Oceanic Sciences, Institute of Atmospheric Sciences, Fudan University, Shanghai, China, [3]Center for Analysis and Prediction of Storms, University of Oklahoma, Norman, OK, USA, [4]Shanghai Carbon Data Research Center, CAS Key Laboratory of Low-Carbon Conversion Science and Engineering, Shanghai Advanced Research Institute, Chinese Academy of Sciences, Shanghai, China, [5]Shanghai Environmental Monitoring Center, Shanghai, China, [6]Key Laboratory of Environmental Optics and Technology, Anhui Institute of Optics and Fine Mechanics, Hefei Institutes of Physical Science, Chinese Academy of Sciences, Hefei, China, [7]Zhejiang Lin'an Atmospheric Background National Observation and Research Station, Hangzhou, China, [8]Shanghai Meteorological Service, Shanghai, China, [9]Shanghai Key Laboratory of Meteorology and Health, Shanghai, China, [10]Shanghai Qi Zhi Institute, Shanghai, China, [11]Institute of Eco-Chongming (SIEC), Shanghai, China, [12]Multiphase Chemistry Department, Max Planck Institute for Chemistry, Mainz, Germany

Abstract While the reduction in anthropogenic emissions due to Coronavirus disease 2019 (COVID-19) lockdown in China and its impact on air quality have been reported extensively, its impact on ambient carbon dioxide (CO_2) concentrations is still yet to be assessed. In this study, the impact of emission reductions on spatiotemporal changes of CO_2 concentrations during the COVID-19 pandemic was quantified in the Yangtze River Delta region (YRD), using high-resolution dynamic emission inventory and the Weather Research and Forecasting model coupled with the Vegetation Photosynthesis and Respiration Model (WRF-VPRM). The simulated CO_2 concentrations from dynamic emission inventory shows a better agreement with surface observations compared with the Open-source Data Inventory for Anthropogenic CO_2 and Emission Database for Global Atmospheric Research emission, providing confidence in the quantification of CO_2 concentrations variations. Our results show that emission reductions during the COVID-19 pandemic lead to a CO_2 decrease by 4.6 ppmv (−1.1%) in Shanghai and 3.1 ppmv (−0.7%) in YRD region. For the column-averaged CO_2 concentrations (denoted as XCO_2), it also decreases by 0.20 ppmv (−0.05%) in Shanghai and 0.15 ppmv (−0.04%) in YRD region. Furthermore, emission reductions from transportation and industry are major contributors to the decline in CO_2 concentrations at the near surface, accounting for 45.8% (41.1%) and 34.9% (41.0%) in Shanghai (YRD). Our study deepens the understanding of the response of CO_2 concentrations to different sectors, which is helpful for emission management and climate adaption policies.

Plain Language Summary Carbon dioxide (CO_2) is the most important greenhouse gas in the atmosphere and has a profound impact on global climate change. It kept increasing over the last decades. Although previous studies have investigated the sources and sinks of air pollutants, the variations of CO_2 concentrations at regional to national scales remains poorly understood owing to a lack of long-term observations and limited modeling studies. High-resolution CO_2 emission inventory is in high demand in accurate CO_2 simulations. This work integrates a high-resolution dynamic emission inventory with WRF-VPRM model to quantify the influence of reduced emissions from different sectors on the spatiotemporal changes of CO_2 concentrations during the COVID-19 pandemic. This modeling system can help to understand the response of CO_2 concentrations to emissions and serves as a basis for atmospheric inversion of CO_2 emissions.

1. Introduction

The rising carbon dioxide (CO_2) emissions significantly contribute to global warming (IPCC, 2007). To mitigate the global warming, the Paris Agreement sets the goal of keeping global warming well below 2°C, with efforts

Validation: Chong Wei
**Writing – original draft:** Yanyu Wang
Writing – review & editing: Cheng Huang, Xiao-Ming Hu, Hang Su, Renhe Zhang

to limit warming to 1.5°C above preindustrial levels to reduce greenhouse gas emissions (IPCC, 2018). CO_2 has many natural and anthropogenic sources and sinks, and there is much uncertainty in quantifying its regional and global assessments (Eldering et al., 2017; Schwandner et al., 2017). A better understanding of its sources and sinks as well as the response of CO_2 concentrations to their emissions are crucial for the Carbon Neutralization Strategy in China.

In the first half of 2020, the unprecedented worldwide lockdown caused by the coronavirus disease 2019 (COVID-19) pandemic resulted in significant reductions in global energy consumption and CO_2 emissions. Current estimates suggested that global CO_2 emissions decreased by 8.6% from January to April 2020 (Le Quéré et al., 2020). In China, CO_2 emissions decreased by 7%, with ground transportation emissions falling by 53% (Z. Liu et al., 2020; Zheng et al., 2020). Surface observations also witnessed the reduction in CO_2 concentrations during the COVID-19 pandemic in cities such as San Francisco (USA), Los Angeles (USA), Florence (Italy), Anmyeondo (Korea), Beijing (China), Xi'an (China) and Waliguan (China) (Sim et al., 2022; Turner et al., 2020; Venturi et al., 2021; Wu et al., 2021; Xie et al., 2022; Yadav et al., 2021; Zeng et al., 2022). However, it is still challenging to identify the impact of the emissions' signal on CO_2 concentrations during the COVID-19 pandemic. This is because CO_2 is long-lived, COVID-related CO_2 variations are relatively small on top of a large background, typically only 1–10 ppmv (0%–0.5% of 400 ppmv), which may be below the measurement precision of surface observations or satellite data (Dacre et al., 2021). It is demonstrated that satellite-based observations (e.g., OCO-2 and GOSAT (The Greenhouse Gases Observing Satellite)) are difficult to detect the reduction in the column-averaged CO_2 concentrations (denoted as XCO_2) during the COVID-19 pandemic (Buchwitz et al., 2021; Chevallier et al., 2020). On the other hand, CO_2 concentrations are strongly influenced by many factors, including weather patterns, biological sinks and background CO_2 fluctuations (Hu et al., 2020; Keeling et al., 1996). To eliminate the impacts of weather conditions and background fluctuations on CO_2 concentrations, for example, D. Liu et al. (2021) used similar weather conditions to identify the impact of anthropogenic emissions on the on-road CO_2 concentrations in Beijing. Monteiro et al. (2022) used some observational metrics, including the enhancement of CO_2 concentrations in urban site relative to background site, the amplitude of diurnal cycle and vertical gradients, to identify the reductions in CO_2 concentrations caused by the COVID-19 pandemic. Nevertheless, many uncertainties still exist to infer COVID-related CO_2 enhancement from observations, particularly in urban areas with high CO_2 emissions and complex sources (Lian et al., 2023).

Numerical simulation is a useful tool to identify the impact of COVID-related emissions on regional CO_2 concentrations. An online CO_2 weather-biosphere coupled model has been developed with considering the feedbacks between biosphere processes and meteorology conditions in one coordinate system (Ahmadov et al., 2007). The subsequent study indicated that this model, the Vegetation Photosynthesis and Respiration Model (VPRM) into the Weather Research and Forecasting (WRF) model (WRF-VPRM), can capture the dynamic changes of CO_2 concentrations, and its performance is better than other global models (Ahmadov et al., 2007; Mahadevan et al., 2008). Many researches have been paid attention to the application and validation of WRF-VPRM model in North America (Hu et al., 2020, 2021b) and Europe (Pillai et al., 2010, 2011). Over China, Diao et al. (2015) first evaluated WRF-VPRM model compared with three sites during 5-day period in 2010. Based on modeling and observations, X. Li et al. (2020) analyzed the variations of terrestrial CO_2 fluxes over mixed forest and rice paddy areas in Northeast China. Dong et al. (2021) conducted long-term simulations to investigate the daily, seasonal and yearly variations of CO_2 concentrations in Eastern China. These studies have shed light on deepening the understanding in the characteristics of anthropogenic and biogenic CO_2 concentrations in China. However, these evaluations were limited to comparisons with spatially sparse observations in rural areas over China, model performance in urban areas is still lacking to date. In addition, during the last two decades, many efforts have been devoted to improving CO_2 simulations, including better physical parameterization scheme, biosphere processes and anthropogenic emission inventory (Park et al., 2018, 2020; Pillai et al., 2011). For example, Kretschmer et al. (2012) found that planetary boundary layer (PBL) parameterization schemes in the models can potentially impact the simulations of CO_2 vertical mixing profiles. Through updating the parameterization of terrestrial flux in models, Hu et al. (2020) improved the simulation of nighttime CO_2 peaks. Moreover, S. Feng et al. (2016) suggested high-resolution anthropogenic emission inventory is crucial for accurate CO_2 simulations, especially in urban areas. In China, previous studies usually used global and open-source CO_2 emission inventory in the CO_2 simulations, such as the Open-source Data Inventory for Anthropogenic CO_2 emission (ODIAC) and Emission Database for Global Atmospheric Research (EDGAR) (e.g., Diao et al., 2015; Dong et al., 2021; Hu et al., 2021b; X. Li et al., 2020). Compared with EDGAR, Hu et al. (2020) indicated that ODIAC leads to better performance in
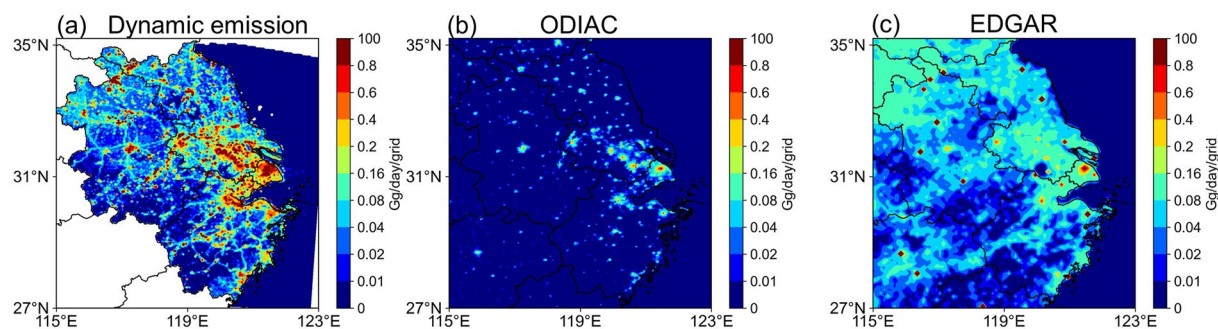
Figure 1. Averaged daily CO_2 emission intensity (unit: Gg/day/grid) in Yangtze River Delta region (YRD) during the COVID-19 pandemic for (a) CO_2 dynamic emission (4 × 4 km), (b) the Open-source Data Inventory for Anthropogenic CO_2 (ODIAC) (1 × 1 km), (c) Emission Database for Global Atmospheric Research (EDGAR) (0.1° × 0.1°).

the CO_2 simulations, particularly in large urban areas. Che et al. (2022) found that ODIAC was overestimated CO_2 concentrations compared with the observations in Beijing while EDGAR resulted in underestimation. Therefore, the evaluation of different anthropogenic emission is urgently needed in Yangtze River Delta (YRD) region, and it serves as a basis for accurate quantification of the anthropogenic signal's impact on CO_2 concentrations during the COVID-19 pandemic over YRD region.

YRD region is one of the highest population density and highest CO_2 emissions areas with densely distributed industries and transportation in China. Many efforts have been made to investigate the air pollution during the COVID-19 pandemic (H. Wang et al., 2022; X. Wang & Zhang, 2020), however, the variations of CO_2 concentrations are still unclear in YRD region. Moreover, high-resolution CO_2 simulations is highly needed to better support the mitigation measures and policies. In this study, a high-resolution, dynamic emission inventory and atmospheric transport model (WRF-VPRM) were used to quantify the impact of emission reductions on spatiotemporal changes of CO_2 concentrations during the COVID-19 pandemic. YRD region is our study area and it includes Shanghai, Jiangsu, Anhui and Zhejiang Provinces. Our study period is the COVID-19 pandemic (from 1 January to 31 March 2020). It provides a good opportunity to examine the performance of CO_2 models, and to investigate CO_2 concentrations in response to emission reductions from different sectors that have been completely or partially removed. The goals of this study are to: (a) assess the performance of CO_2 dynamic emission inventory and the suitability of WRF-VPRM model in YRD region; (b) quantify the impact of emission reductions and meteorology on CO_2 (XCO_2) concentrations during the COVID-19 pandemic; (c) explore the contribution of different anthropogenic sectors to spatiotemporal changes of CO_2 concentrations. This paper is organized as follows. The data and method are described in Section 2. Section 3 presents the model validation and the COVID-related changes in CO_2 concentrations. The conclusion and discussion are in Section 4.

2. Materials and Methods

2.1. Anthropogenic CO_2 Emission Inventory

Three anthropogenic emission inventories were used in this study, including dynamic emission inventory (hereafter named as dynamic emission), ODIAC and EDGAR (Figure 1). Dynamic emission inventory was developed to characterize the daily emission changes during the COVID-19 pandemic based on real-time activity data from multi sources (Figure 1a, Huang et al., 2021). These real-time activity data were normalized to establish a set of dynamic temporal allocation coefficients and then are multiplied by baseline emissions for each subcategory (Figure S1 in Supporting Information S1). The baseline emission inventory was conducted mainly using bottom-up method, which employs emission factors and activity data based on reliable and city-level emission database to map gridded emissions. More details of baseline emission inventory and its assessment can be found in An et al. (2021), and it was also used in some air quality studies over YRD region (e.g., Z. Liu et al., 2020; H. Wang et al., 2022).

Dynamic emission inventory covers five major categories, including power plants, heavy industry, light industry, mobile source and the others, and 25 subcategories. Specifically, daily industrial emission was estimated by continuous emission monitoring system and industrial electricity consumption data. The emissions from gasoline
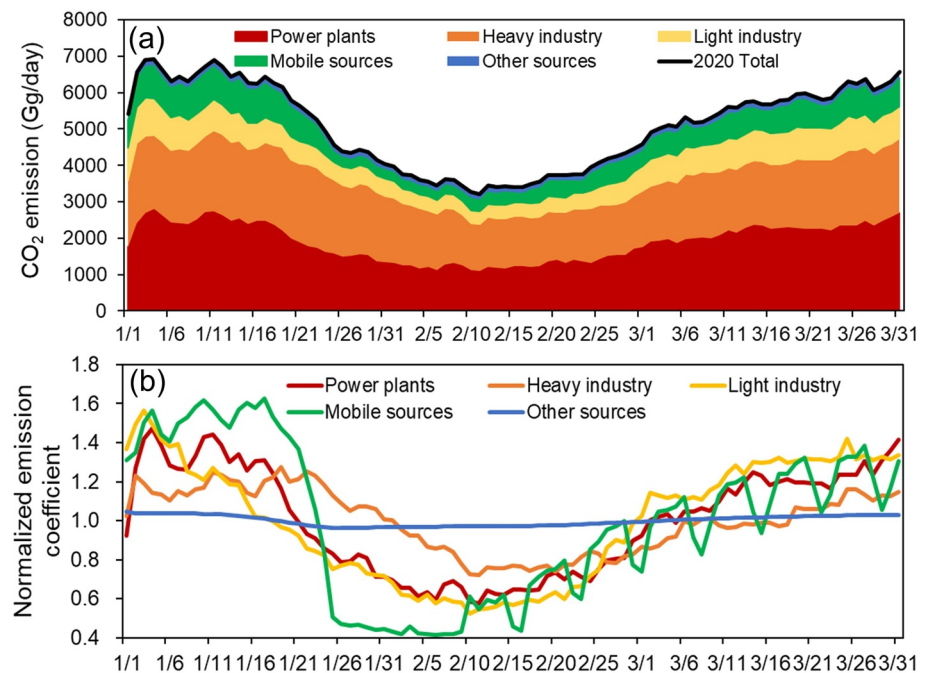
Figure 2. (a) Time series of total CO_2 emission and from CO_2 dynamic emission inventory in Yangtze River Delta region (unit: Gg/day) for power emission (red), heavy industrial emission (orange), light industrial emission (yellow), transportation emission (green) and other sources (blue). (b) Time series of normalized coefficients of different sectors.

and diesel vehicles were assessed using real-time traffic flow data. Transportation emissions were characterized by real-time monitored vehicle flow, ship automatic identification system and aircraft land take-off data (Figure S1 in Supporting Information S1). The daily variations of five major sector from dynamic emission during the COVID-19 pandemic are shown in Figure 2a, their daily normalized coefficients are calculated in Figure 2b. Heavy industry and light industry are summed as industrial sector, the variable of other sources is mainly residential sector during the COVID-19 pandemic, and thus dynamic emission was further grouped into four major source categories, including power plants (Power), industrial (Ind), transportation (Trans), and residential (Res) emissions for further analysis. Dynamic emission is covered YRD region with spatial resolution of 4×4 km. The emissions outside of YRD region are from ODIAC.

ODIAC is developed by the National Institute for Environmental Studies, which was estimated from the Carbon Dioxide Information Analysis Center and British Petroleum (BP), using proxy of data including satellite-observed nighttime light and point source emissions (Oda et al., 2018, 2019). The version of ODIAC2022 provides global and monthly anthropogenic emissions of CO_2 for 2020 with the spatial resolution of 1×1 km (Figure 1b).

EDGAR provides global gridded CO_2 emission and the national emissions are from the energy balance statistics of the International Energy Agency, and country-specific activity data sets come from BP, World Steel Association, Global Gas Flaring Reduction Partnership/U.S. National Oceanic and Atmospheric Administration and United States Geological Survey (Crippa et al., 2022a). The spatial disaggregation of national emissions was based on proxy data including population density, nighttime lights, traffic networks and CO_2-emitting point sources. EDGARv7.0 can provide monthly emissions for 2020 and it has a spatial resolution of $0.1° \times 0.1°$ (Figure 1c). These three emission inventories are re-gridded into the same spatial resolution as the WRF grid based on bilinear interpolation.

2.2. Model Configurations

A weather-biosphere-online-coupled model, the Weather Research and Forecasting model (WRF, version 4.0) coupled with the VPRM, was used in this study. It can identify and label CO_2 concentrations from anthropogenic emission, terrestrial biogenic flux and background condition as ANT, BIO, BCG respectively, based on CO_2 fluxes from terrestrial biogenic fluxes and anthropogenic emissions (Ahmadov et al., 2007; Hu et al., 2020).
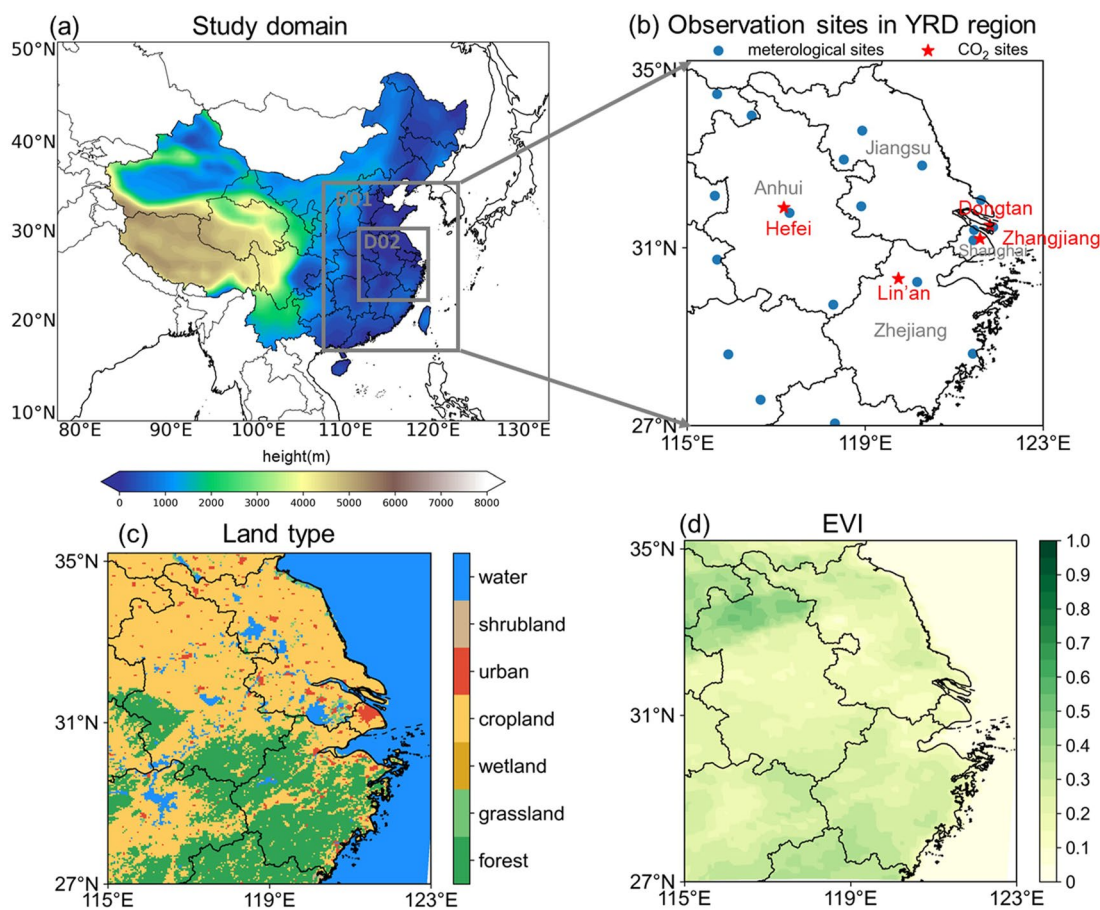
Figure 3. (a) The study domain of Weather Research and Forecasting model coupled with the Vegetation Photosynthesis and Respiration Model model. (b) The locations of meteorological sites (blue dots) and four CO_2 sites (red stars) in Yangtze River Delta (YRD) region, including Zhangjiang (in Shanghai), Dongtan (in Shanghai), Lin'an (in Zhejiang Province) and Hefei (in Anhui Province). (c) Land types in YRD region. (d) Enhanced Vegetation Index (EVI) derived from MODerate Resolution Imaging Spectroradiometer (MODIS) (the MODIS) in YRD region.

VPRM model was used to calculate the terrestrial biogenic fluxes with considering the ecosystem respiration (ER) and gross ecosystem exchange (Mahadevan et al., 2008). To better simulation of CO_2 biogenic fluxes, an improved terrestrial respiration parameterization developed by Hu et al. (2021b) was adopted in this study. It is incorporated Enhanced Vegetation Index (EVI), water stress scaling factor and a quadratic dependence on surface air temperature (Gourdji et al., 2022), to replace the old ER parameterization in VPRM, which is simply a linear function of temperature. Table S1 in Supporting Information S1 shows the VPRM parameters used in this study. Satellite observation (the MODerate Resolution Imaging Spectroradiometer (MODIS) provides inputs to VPRM, including vegetation fractions, EVI and Land Surface Water Index (LWSI). Seven categories of vegetation fractions, including deciduous forest, evergreen forest, mixed forest, shrubland, savannah, cropland and grassland, were derived from MODIS land cover type product (MCD12Q1, Friedl et al., 2002), just as shown in Figure 3c. EVI (Figure 3d) and LWSI were calculated from 8-day MODIS land surface reflectance data (MOD09A1). The spatial resolution of these MODIS products is 500 m and they are re-gridded to match the model grids. In addition, climatological monthly ocean CO_2 fluxes are also incorporated into our WRF-VPRM simulations (Takahashi et al., 2009). Initial and lateral boundary conditions of atmospheric CO_2 were from global inversion-optimized CO_2 concentrations based on satellite provided by the Copernicus Atmosphere Monitoring Service (CAMS) (Agustí-Panareda et al., 2023).

The WRF-VPRM model was configured with two domains (WRF, version 4.0), East China and nested YRD region (Figure 3), with the outer domain having a spatial resolution of 12 km and the inner domain having a spatial resolution of 4 km to match the spatial resolution of CO_2 dynamic emission inventory. The model has 47 vertical layers. Initial and boundary conditions for meteorological variables are from the National Center

Table 1
Description of Model Experiments in This Study

Experiment	Anthropogenic emission	Meteorology
Dynamic Emission (S0)	Dynamic emission for 2020	2020
ODIAC	ODIAC	2020
EDGAR	EDGAR	2020
S2	Dynamic emission for 2020	2019
S3	Dynamic emission for 2019	2020
S4	Power emission is from 2020 dynamic emission, other sectors are 2019	2020
S5	Industrial emission is from 2020 dynamic emission, other sectors are 2019	2020
S6	Transportation emission is from 2020 dynamic emission, other sectors are 2019	2020
S7	Residential emission is from 2020 dynamic emission, other sectors are 2019	2020

for Environmental Prediction's Final Analysis data set with a horizontal resolution of $1° \times 1°$. Model configuration here is similar with that of Hu et al. (2020) and X. Li et al. (2020). The physical schemes used in our study include Noah land surface scheme (Chen & Dudhia, 2001), Dudhia short wave radiation (Dudhia, 1989), rapid radiative transfer model (RRTM) long wave radiation (Mlawer et al., 1997), Grell-3 cumulus scheme (Grell & Devenyi, 2002), and the Yonsei University (YSU) PBL scheme (Hong et al., 2006). Following Hu et al. (2017, 2018, 2021b), this study employs spectral nudging and climatic downscaling techniques. Throughout the downscaling simulation, the variables, including geopotential height, temperature and horizontal wind components, are spectrally nudged to the reanalysis data. The detailed configurations are summarized in Table S2 in Supporting Information S1. The simulation was conducted during the COVID-19 pandemic, from 1 January to 31 March 2020, with the first 3 days serving as the spin-up period, so only 4 January to 31 March 2020 were considered. Furthermore, the COVID-19 pandemic was divided into three period: 4–24 January was before the lockdown (PRE), 25 January to March 10 was the lockdown (LOCK), and March 11 to March 31 was the resumption of work (RS).

2.3. Model Experiment Design

Several numerical experiments were designed to isolate the impact of meteorology and emission reduction on ambient CO_2 concentrations during the COVID-19 pandemic (Table 1). To examine the performance of different emission inventories in CO_2 simulations, three experiments were conducted first. (a) Dynamic Emission case (S0), in which anthropogenic emission inventory is from dynamic emission for the year 2020; (b) ODIAC case, in which anthropogenic emission inventory is from ODIAC; (c) EDGAR case, in which anthropogenic emission inventory is from EDGAR.

After evaluating the performance of dynamic emission in CO_2 simulation, two experiments were designed to distinguish the impact of emission reductions and meteorological conditions on CO_2 concentrations: (a) S2, driven by 2019 meteorology, the difference between S2 and S0 is the impact of meteorology; (b) S3, driven by 2019 dynamic emission and 2020 meteorology, the difference between S3 and S0 is the impact of emission reductions. Furthermore, the absolute ratio of (S2–S0)/(S3–S0) was calculated to quantify the weight between meteorology impact and emission reduction impact.

To quantify the source contribution of each emission sector to CO_2 concentrations, four additional experiments were carried out (S4–S7), power (industrial/transportation/residential) emission is from 2020 dynamic emission respectively, while other sectors are from 2019 dynamic emission. The difference of CO_2 concentrations between S4 (S5/S6/S7) and S3 denotes the impact of power (industrial/transportation/residential) emission reduction on CO_2 concentrations in 2020 compared with in 2019.

2.4. CO₂ Surface Measurements

Hourly measurements of CO_2 concentrations during January–March 2020 were collected at four sites to validate the model results, and the location of these sites are shown in Figure 3b (red stars). One of two sites located in

Table 2
Statistical Results for Simulated and Observed Meteorological Variables in Yangtze River Delta Region

Index[a]	T2 (°C)	RH (%)	WS10 (m/s)	WD10 (°)
MB[b]	−0.94	1.61	0.60	−7.53
RMSE[c]	1.99	12.09	1.12	−40.28
R[d]	0.94	0.80	0.75	–

Note. T2, temperature at 2 m (°C); RH, relative humidity at 2 m (%); WS10, wind speed at 10 m (m/s); WD, wind direction at 10 m (deg). Note that the metrics include mean bias (MB), root-mean-square error (RMSE) and correlation coefficient (R). [a]In the equations, sim and obs represent the simulated and observed temperature, and N is the number of data pairs at all the observation sites. [b]$MB = \frac{1}{N}\sum_{i=1}^{N}(\text{sim}_i - \text{obs}_i)$. [c]$RMSE = \sqrt{\frac{1}{N}\sum_{i=1}^{N}(\text{sim}_i - \text{obs}_i)^2}$. [d]$R = \frac{\sum_{i=1}^{N}\left(\text{sim}_i - \overline{\text{sim}}\right)\left(\text{obs}_i - \overline{\text{obs}}\right)}{\sqrt{\sum_{i=1}^{N}\left(\text{sim}_i - \overline{\text{sim}}\right)^2 \sum_{i=1}^{N}\left(\text{obs}_i - \overline{\text{obs}}\right)^2}}$.

Shanghai, at Zhangjiang (urban site, 121.59°E, 31.18°N), and Dongtan (a rural site located in Chongming island, 121.88°E, 21.47°N). CO_2 concentrations were measured by Picarro G2301 spectrometer, with routinely quality control (Wei et al., 2020). Lin'an Regional Atmospheric Background Station (rural site, 119.75°E, 30.30°N) in Zhejiang Province can provide hourly measurements of CO_2 concentrations during our study period. In addition, one of Total Carbon Column Observing Network site-Hefei in Anhui Province (rural site) was also used to validate modeled CO_2 concentrations (W. Wang et al., 2017), which provides available CO_2 concentrations with 35 days during PRE and RS of COVID-19 pandemic. These data have been quality control and they were calculated as hourly mean value.

2.5. CO_2 Aircraft Observations

CONTRAIL (Comprehensive Observation Network for Trace gases by Airliner) program provides CO_2 concentrations in vertical profiles between ∼1 and ∼8 km above ground level (AGL), and a Continuous CO2 Measuring Equipment for in-situ CO_2 measurements was installed on the airplane (Machida et al., 2008). Two days of CO_2 vertical profiles during our study period (31 January and 7 February) were used for the model evaluation during aircraft landings and takeoffs near the Shanghai airport.

2.6. Meteorological Measurements

Meteorological variables, including air temperature (T) and relative humidity (RH) at 2 m, wind speed (WS) and wind direction (WD) at 10 m, were obtained from national meteorological observing station by the China Meteorological Administration, to be used to validate the meteorological performance of WRF-VPRM model. Twenty-two meteorological sites in our study domain were selected and their locations are shown in Figure 3b (blue circles).

3. Results

3.1. Model Validation

3.1.1. Meteorological Evaluations

Meteorological conditions play crucial roles in biogenic CO_2 production, CO_2 transportation and dispersion (Hu et al., 2021a). We first compared the simulated near-surface temperature (T), RH, WS and WD with 22 meteorological stations in YRD region to evaluate the model performance. On averages, the model slightly underestimates the temperature, with mean bias (MB) of −0.94°C and root-mean-square error (RMSE) of 1.99°C; RH is slightly overestimated in most areas except the north areas of YRD region, with MB of 1.61% and RMSE of 12.09%; WS is generally overestimated, with MB of 0.6 m/s and RMSE of 1.12 m/s; for WD, the model has a more bias than above variables, with MB of −7.53° and RMSE of 40.28° (Table 2). The spatial statistics plots, including MB, RMSE and correlation coefficient (R), are shown in Figure S2 in Supporting Information S1, indicating WRF-VPRM model has a good agreement with the surface observations.

3.1.2. Comparisons With Surface CO_2 Measurements

To evaluate the performance of different anthropogenic emissions in the CO_2 simulation, simulated CO_2 concentrations from dynamic emission, ODIAC and EDGAR were compared with the surface measurements in four sites over YRD region (Figure 4). The simulated CO_2 concentrations in Dynamic Emission case at all sites are more consistent
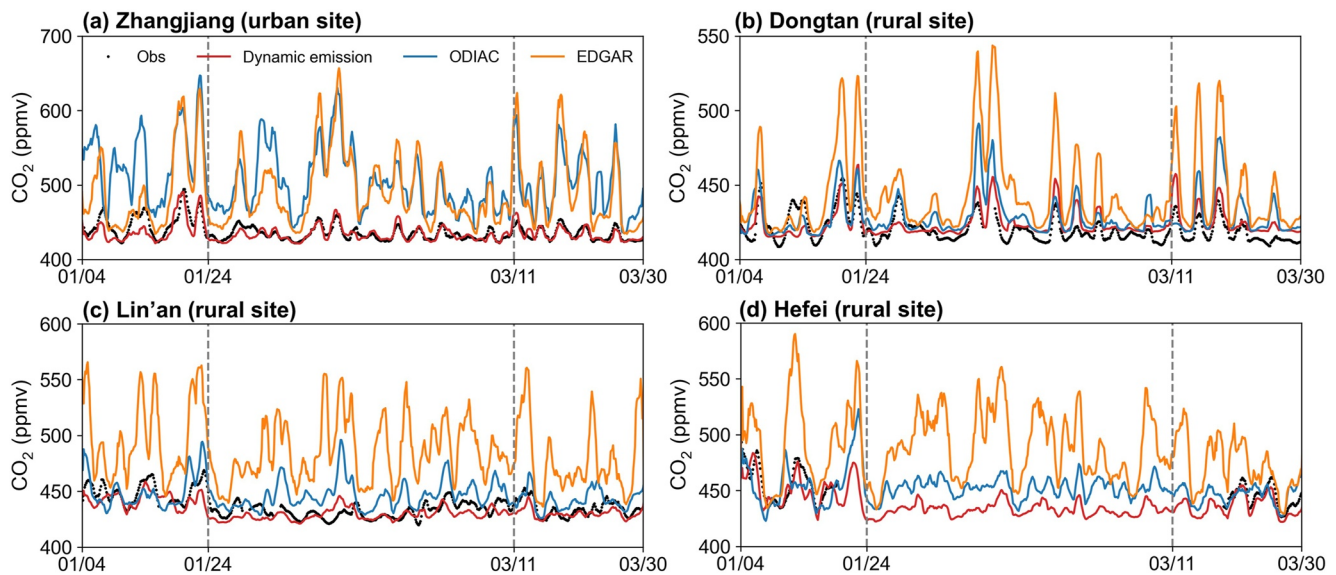
Figure 4. Time series of simulated CO_2 concentrations from dynamic emission (red line), Open-source Data Inventory for Anthropogenic CO_2 (ODIAC) (blue line) and Emission Database for Global Atmospheric Research (EDGAR) (orange line), compared with observations (black dots) at four sites, (a) Zhangjiang, (b) Dongtan, (c) Lin'an, (d) Hefei. Note that Hefei has only 35-day CO_2 observations during PRE and RS of COVID-19 pandemic.

with observations, with MB (RMSE) falls in the range of −4.9~2.5 (8.5~12) ppmv (Table 3). Furthermore, Dynamic Emission case can capture the fluctuations in CO_2 concentrations brought on by lockdown, with a rapid response to the start of lockdown on 24 January and a minor recovery during RS, especially at Zhangjiang (Figure 4a) and Lin'an site (Figure 4c). However, ODIAC and EDGAR both show a large bias in four sites, especially for EDGAR, its emission intensities were overestimated and they are about 1.5~3 times higher than dynamic emission. It is also found that high emissions can be found in some single grid cells of EDGAR in Figure 1c, which may be overestimated. Han et al. (2020) also pointed out that EDGAR greatly overestimated CO_2 emissions in urban areas over China compared with other emission inventories. ODIAC overall has a better performance than EDGAR in three rural sites (Dongtan, Lin'an and Hefei), but its emission intensity was overestimated with ~2 times higher than dynamic emission at Zhangjiang. Furthermore, both EDGAR and ODIAC distribute national emissions to gridded emissions, while our local emission (dynamic emission) is based on city-level and more reliable in both total emission estimates and spatial pattern (Huang et al., 2021). As a result, not small discrepancy of gridded emissions still exists among three emission inventories. More CO_2 observations are needed here to evaluate the performance of these emission inventories.

Our results show that using dynamic emission can perform better than that of other pervious CO_2 simulations in urban regions (Table S3 in Supporting Information S1). Table S3 in Supporting Information S1 also shows that accurate simulation of urban CO_2 concentrations is still a challenge, especially in the short-term simulation (e.g., Dong et al., 2021; T. Feng et al., 2019; Liang et al., 2022; C. Liu, 2015). Therefore, high-resolution dynamic emission is very crucial for CO_2 simulations over YRD region.

Compared with PRE, obvious decrease of CO_2 concentrations in urban scales are well captured between Zhangjiang and Dongtan sites located in Shanghai during LOCK (Figure S3a in Supporting Information S1), with dropping by −3.2% (observation) and −2.2% (simulation) at Zhangjiang, and −2.3% (observation) and −0.6% (simulation) at Dongtan (Figure S3a in Supporting Information S1). Meanwhile, observation (model) results shows the difference in CO_2 concentrations in these two sites (urban-rural, ΔCO_2) decrease from 21.8 ppmv (16.1 ppmv, PRE) to 17.1 ppmv (10.6 ppmv, LOCK), implying that CO_2 concentrations from anthropogenic emission decreased during LOCK (Figure S3b in Supporting Information S1). In general, using dynamic emission can greatly improve CO_2 simulations, giving confidence in further analyses to quantify the effect of COVID-19 pandemic on CO_2 concentrations.

3.1.3. Comparisons With Aircraft Observations

Vertical profiles of simulated CO_2 concentrations using dynamic emission are evaluated using the aircraft data from the CONTRAIL campaign during two cases, 31 January and 7 February 2020 (Figure 5). For both cases,

Table 3
Statistical Results for Observed and Simulated CO_2 Concentrations From Dynamic Emission, Open-Source Data Inventory for Anthropogenic CO_2 (ODIAC) and Emission Database for Global Atmospheric Research (EDGAR) Case, at Zhangjiang, Dongtan, Lin'an and Hefei Sites

Index	Zhangjiang			Dongtan		
	Dynamic	ODIAC	EDGAR	Dynamic	ODIAC	EDGAR
MB	−2.33	70.43	68.19	2.50	8.24	22.87
NMB[a]	−0.5%	16.1%	12.4%	0.4%	2.0%	5.4%
RMSE	12.0	93.66	68.19	8.83	13.24	30.85
R	0.78	0.52	0.67	0.70	0.62	0.7

Index	Lin'an			Hefei		
	Dynamic	ODIAC	EDGAR	Dynamic	ODIAC	EDGAR
MB	−4.71	9.93	50.76	−4.93	−0.49	29.31
NMB[a]	−1.1%	2.3%	11.6%	−1.3%	−0.1%	6.5%
RMSE	8.51	16.05	58.13	9.05	16.46	39.24
R	0.72	0.52	0.50	0.84	0.43	0.71

Note. The metrics include mean bias (MB), Normalized mean bias (NMB), root-mean-square error (RMSE) and correlation coefficient (R).
[a]$NMB = \frac{1}{N}\sum_{i=1}^{N}\frac{(sim_i - obs_i)}{obs_i}$.

the WRF/VPRM model nicely reproduces the free troposphere CO_2 variation at ~415 ppm. On 31 January, the model simulation can capture the vertical gradient of CO_2 concentrations across boundary layer top at ~1 km AGL during the flight ascending and descending time. Both the model and observations indicate significant accumulation of CO_2 in the boundary layer, which is due to local CO_2 emissions confined in the boundary layer. On February 7, the model simulation can reproduce the shape of aircraft profile with elevated CO_2 concentration in the boundary layer (~1 km) particularly at 05 UTC, and an elevated CO_2 layer at ~3 km AGL. The concentrations of the elevated CO_2 layer at ~3 km is underestimated. Such an elevated CO_2 layer above the boundary layer is likely due to long range transport. The model-observation discrepancy is partially due to the uncertainties in the meteorological conditions and PBL scheme in the models (Hu et al., 2020). In addition, the difference between models and airplane sampling also could lead to some bias. That is, the model simulates mean profile averaged over grid cells with a 4 km grid spacing, while airplane samples instantaneous state of the atmosphere that is affected by individual turbulent eddies, particularly during an ascent or descent.

3.2. The Impacts of Emission Reductions and Meteorology on CO_2 Concentrations

The impacts of meteorology and emission reductions on CO_2 concentrations were investigated through three model experiments (Dynamic Emission case (S0), S2, S3). As illustrated in Figure 6a, emission reductions owing to the COVID-19 lockdown lead to an obvious decrease in CO_2 concentrations in YRD region, with the peak of −8.5 ppmv. Obvious declines in CO_2 concentrations correspond with high CO_2 emissions along the Yangtze River and Hangzhou Bay, which have the most densely spread industry and transportation (Figure 1a). Meteorology variations promote CO_2 concentrations in Jiangsu and Anhui Province, with maxima reaching ~6 ppmv, while it is somewhat negative in Shanghai and Zhejiang Province (approximately −5 ppmv, Figure 6b). The weather conditions can significantly influence CO_2 fluctuations by air transportation. CO_2 biogenic fluxes also depend on air temperature and solar radiation, even though CO_2 biogenic emission is negligible in winter (Dong et al., 2021). Overall, anthropogenic emission reductions dominate the decrease of CO_2 concentration in almost all YRD region (E > M, C < 0, Figure 6c). Figure 6d demonstrates that emission reductions result in considerable CO_2 reductions of 4.6 ppmv (−1.1%) in Shanghai and 3.1 ppmv (−0.7%) in YRD region. In contrast, changes in meteorological condition have a minor impact on CO_2 concentrations in Shanghai (−0.17 ppmv, −0.04%) and lead to a 0.66 ppmv (0.15%) increase in YRD region.

In addition to surface-level CO_2 concentrations, the impacts of meteorology and emission reductions on XCO_2 were also evaluated (Figure S4 in Supporting Information S1). XCO_2 is strongly influenced by weather patterns and may contain more information about regional-scale flux than the surface. Emission reductions and meteorology have a smaller impact on XCO_2 than at the surface, with approximately 5% of surface-level CO_2 reduction. Anthropogenic emission reduction plays a dominant role in XCO_2 reduction (E > M, C < 0) in YRD region except in some northern parts of Jiangsu and Anhui Province, where meteorology causes a considerable enhancement of XCO_2 increase (M > E, C > 0). In general, emission reductions contribute to a 0.20 ppmv (−0.05%) decrease in XCO_2 in Shanghai and a 0.15 ppmv (−0.04%) decrease in YRD region, while meteorology contributes to a −0.07 ppmv (−0.02%) in Shanghai and 0.03 ppmv (0.01%) in YRD region, respectively.
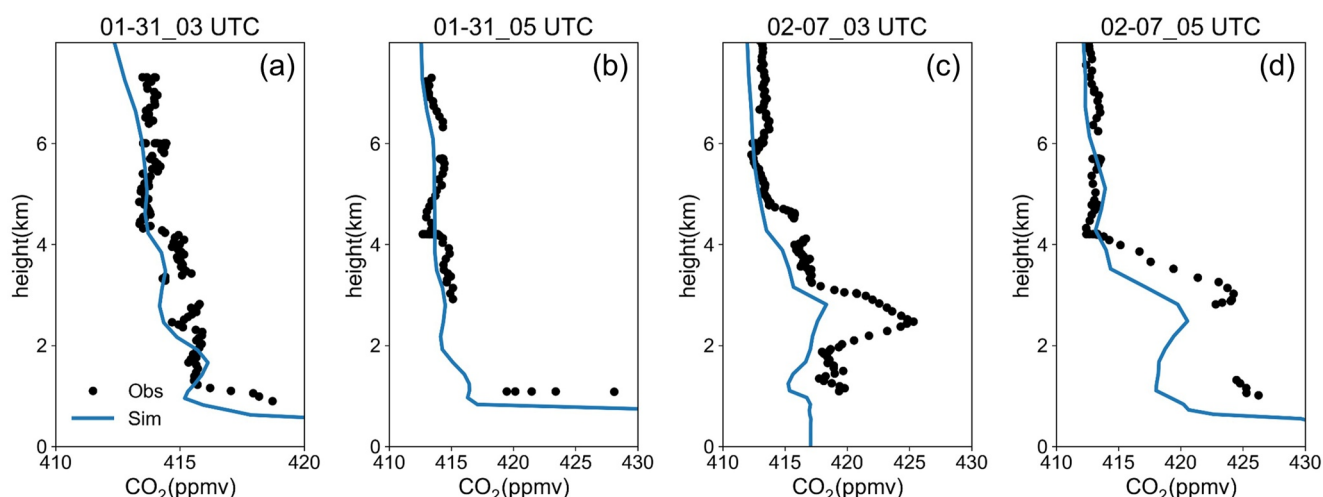
Figure 5. Observed and simulated CO_2 vertical profiles over the Shanghai airport at (a) 0300 UTC on 31 January during one flight descending time, (b) 0500 UTC on 31 January during the other flight ascending time, (c) 0300 UTC on 7 February during descending time, (d) 0500 UTC on 7 February during ascending time.
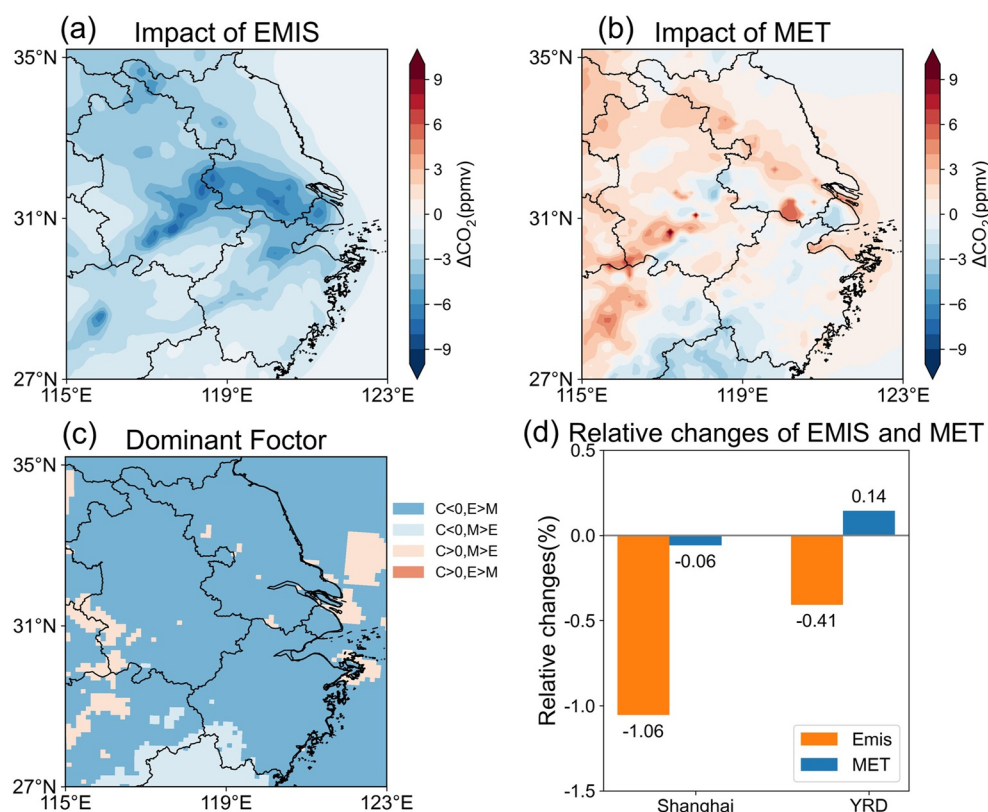
Figure 6. The relative changes in CO_2 concentrations due to emission reduction (EMIS) averaged at LOCK (COVID-19 lockdown, 25 January to 10 March 2020). (b) Same as (a), but for meteorology (MET), (c) dominant factor between emission reduction and meteorology. The label C is the relative changes in CO_2 concentrations during COVID-19 lockdown; E > M indicates emission reduction dominated, M > E refers to meteorology dominated. (d) Averaged relative changes in CO_2 concentrations due to EMIS (orange bar) and MET (blue bar) in Shanghai and Yangtze River Delta (YRD) region during LOCK.
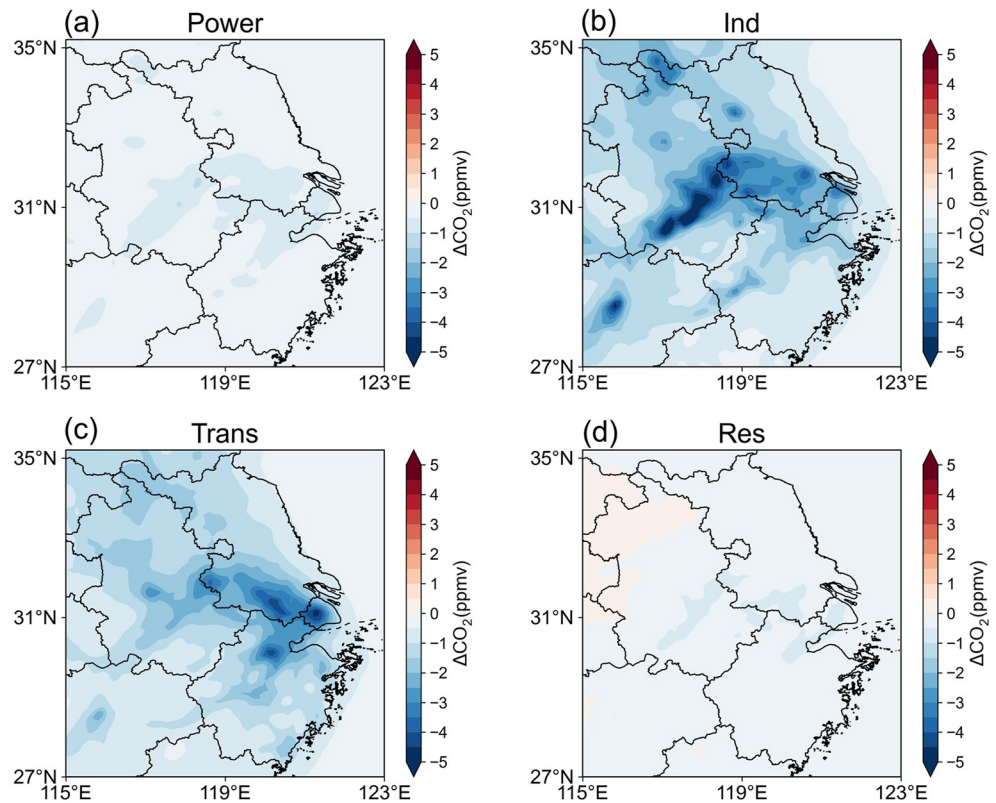
Figure 7. The relative changes in CO_2 concentrations due to the reduction of (a) power emission (Power), (b) industrial emission (Ind), (c) transportation emission (Trans), and (d) residential emission (Res) averaged at LOCK (COVID-19 lockdown, 25 January to 10 March 2020).

3.3. Response of CO_2 Concentrations to Different Sector-Based Reductions

3.3.1. Surface-Level of CO_2 Concentrations

To quantify the contribution of different anthropogenic sources to CO_2 reduction, the spatial patterns of ΔCO_2 response to individual sources reduction are displayed in Figure 7 based on four model experiments (S4–S7). Although power emissions dropped by 40% during the LOCK period in YRD region respectively (Figure 2), the contribution of power emission to the decreased CO_2 concentrations is smaller at the surface-level (Figure 7a) compared to industrial and transportation emissions (Figures 7b and 7c). This is due to that power emission is the elevated source, its impact is larger at higher altitudes than at the near surface. Reduced industrial emission contributes to the reduction in CO_2 concentrations along the Yangtze River, and large reductions occurs in the southern areas of Anhui Province, with a maximum reduction of up to −5.2 ppmv (Figure 7b). Reduced transportation emission produces a large impact on CO_2 reduction in the Hangzhou Bay, especially in urban areas and near the East Sea due to heavy road traffic, aviation and shipping (Figure 7c). The transportation-reduced decline in CO_2 concentrations coincides with the spatial distribution of transportation emissions in YRD region (Figure S5c in Supporting Information S1). Residential sources produce a minor influence along the Yangtze River, while a slightly positive impact on northern Anhui Province (Figure 7d) may due to a small increase in residential heating during the winter (Le Quéré et al., 2020). Aside from source emission, the spatial pattern of CO_2 concentrations is also influenced by the regional transport (T. Feng et al., 2019). In boreal winter, the prevailing wind over YRD region is usually characterized by a strong northwest wind (Wei et al., 2020). As a result, the impact of emission reductions on CO_2 concentrations tends to be transported to the south downwind areas. Figure S6 in Supporting Information S1 presents that the spatial patterns of ΔXCO_2 due to the impact of individual emissions are similar to those of CO_2 concentrations, but the magnitude is much smaller than that of surface-level CO_2 concentrations (Figure 7), with a maximum decrease of −0.25 ppmv in XCO_2 induced by reduced industrial emission.
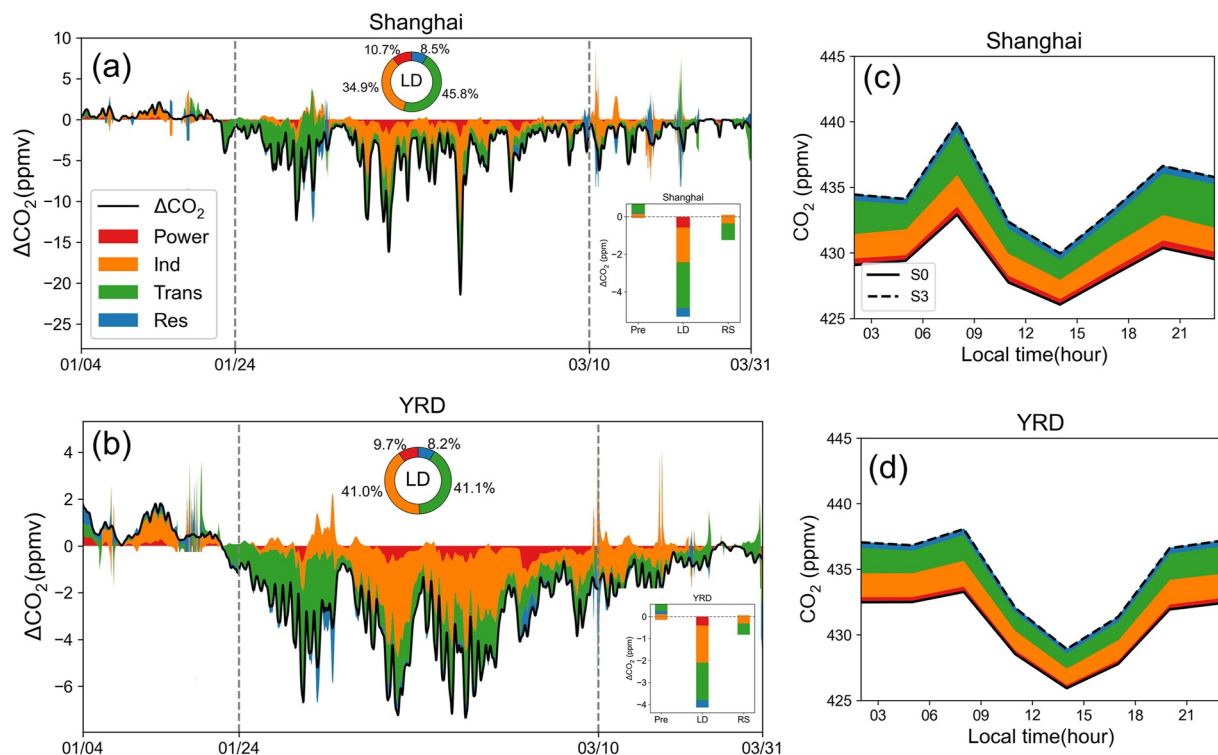
Figure 8. (a) Time series for the contributions of reduced individual sources, including power (red), industrial (orange), transportation (green) and residential (blue) emissions, to CO_2 concentrations during the COVID-19 pandemic in Shanghai. The top of inner panel is the contribution of individual sources to the ΔCO_2 concentrations during LOCK (COVID-19 lockdown, 25 January to 10 March 2020). The right panel is the averaged relative changes of CO_2 concentrations due to the reduction of individual sources during PRE (before the lockdown, 4–24 January 2020), LOCK, and RS (resumption of work, 11–31 March 2020) period. (b) Is same as (a), but for Yangtze River Delta (YRD) region. (c, d) Are averaged diurnal cycle of CO_2 concentrations in Shanghai and YRD region during LOCK.

Figure 8 depicts the temporal variations of the difference in CO_2 concentrations between S0 and S3 (denotes ΔCO_2 due to emission reductions). CO_2 concentrations respond quickly to reduced transportation emission after the lockdown begins (Figure 2), and then the contributions of industrial and power emissions to CO_2 reduction gradually increase in both Shanghai (Figure 8a) and YRD (Figure 8b). During LOCK, the average CO_2 reduction caused by emission reductions is −4.8 ppmv with the maximum reaching 24.5 ppmv in Shanghai. Overall, in Shanghai, the largest contributor of emissions to CO_2 reduction during the LOCK come from transportation (45.8%) and industrial emissions (34.9%), with slightly smaller decreases from power (10.7%) and residential sector emissions (8.5%). In YRD region, mean CO_2 concentrations drop by −1.8 ppmv, with a maximum of −3.5 ppmv, emission contributions are 41.0%, 41.1%, 9.7%, and 8.2%, respectively, for the industrial, transportation, power and residential emissions.

The diurnal variation of CO_2 concentrations in Shanghai (Figure 8c) exhibits a typical urban profile, with two peaks during the rush hours (~8:00 and ~19:00). This characteristic of simulated diurnal cycle is consistent with the surface observation in Shanghai (Wei et al., 2020) and Hangzhou (Pu et al., 2018) during winter. CO_2 peaks during the rush hours are primarily influenced by emission activities. CO_2 concentrations decrease at the noon with the increase of PBL height (PBL), and then it accumulates during midnight with shallower vertical mixing due to lower boundary layer height (PBL). The diurnal cycle of CO_2 concentrations in YRD region (Figure 8d) has no prominent bimodal curve, and it has a negative phase with PBL, with a minor effect of emission activities and plant photosynthesis/respiration processes in winter (Pu et al., 2014). The amplitude of diurnal cycle denotes as the difference between the maximum and the minimum concentrations, and it decrease by 3.14 ppmv in Shanghai and 1.80 ppmv in YRD region between S3 and S0, indicating higher decline in anthropogenic emissions in Shanghai during the COVID-19 pandemic. Moreover, in Shanghai, a considerable decrease (S3–S0) is found in two peaks, due to a large decrease in transportation emission (Figure 8c) during the COVID-19 pandemic. This pronounced decrease was also observed in San Francisco, primarily due to a 48% reduction in traffic emission inferring from CO_2 observations (Turner et al., 2020).
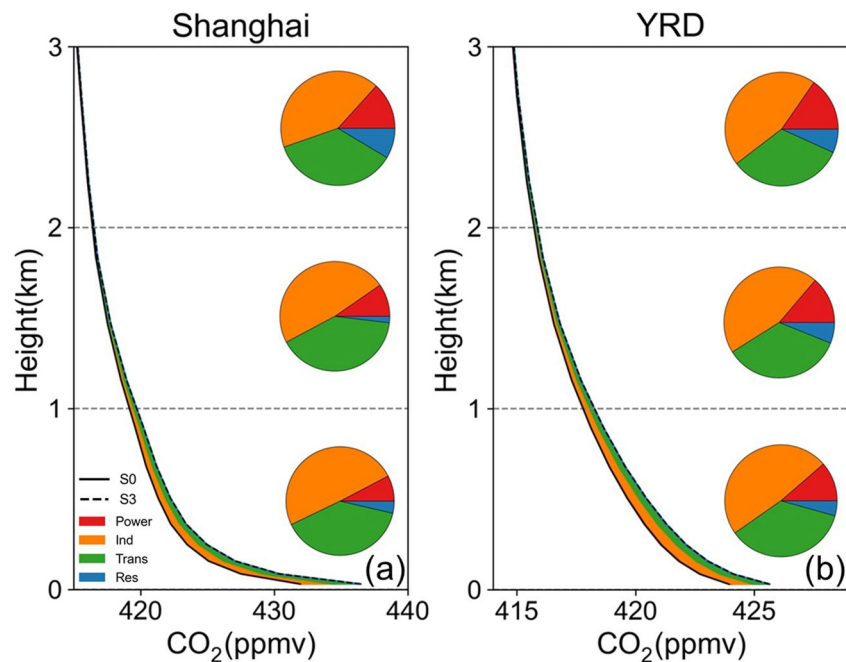
Figure 9. The vertical layer of CO_2 concentrations in (a) Shanghai and (b) Yangtze River Delta (YRD) region. The pies in panel (a) and panel (b) is the averaged contribution of individual sources (power, industrial, transportation and residential emissions) to CO_2 concentrations during LOCK in 0–1 km, 1–2 km and 2–3 km respectively.

3.3.2. Vertical Distribution of CO_2 Concentrations

Figure S7 in Supporting Information S1 presents vertical cross sections of ΔCO_2 concentrations caused by different emissions along AA′ (Figure S8 in Supporting Information S1), where large anthropogenic CO_2 emissions are concentrated along AA′. Due to that there are not point emissions from power plants along AA′, the impact of power emission on CO_2 concentrations is almost completely ignored (Figure S7a in Supporting Information S1). Reduced industrial and transportation emissions are still major contributions to CO_2 concentrations reduction along AA′. Their impacts are very prominent within PBL (black line in Figure S7 in Supporting Information S1) and decrease with increasing height, with up to 2 km in the vertical dimension. Residential emission (Figure S7d in Supporting Information S1) raises CO_2 levels in western areas (Anhui Province), particularly above the PBL. It can be attributed to an increase in home cooking in Anhui province during the COVID-19 lockdown.

The vertical profile of CO_2 concentrations represents a decreasing trend with increasing height (Figure 9), and it drops sharply within PBL with a background concentration of 400+ ppmv. This monotonically decreasing pattern with altitude is consistent with balloon-based observation in Xiamen conducted by Y. L. Li et al. (2014). This pattern usually occurs with stable atmosphere dominant during wither, while in summer, CO_2 concentrations sometimes can be lower near the surface than at elevated altitude because high uptake of CO_2 due to vegetation photosynthesis (Esteki et al., 2017). CO_2 vertical profiles are closely related with vertical variations of meteorological elements (e.g., potential temperature, wind and PBL) and source emissions. Higher levels of CO_2 concentrations accumulate near the surface in Shanghai (Figure 9a) due to anthropogenic emissions sources, and it decreases more within PBL than YRD region (Figure 9b). Both over Shanghai and YRD region, the impact of emission reductions on CO_2 concentrations is remarkable near the surface and it decreases with increasing height. The major contribution is from reduced industrial and transportation emissions. Reduced industrial emissions account for 49.5% (0–1 km), 48.2% (1–2 km), and 42.0% (2–3 km) in Shanghai, and 48.4% (0–1 km), 45.2% (1–2 km), and 43.1% (2–3 km) in YRD region. The contribution of transportation emissions to vertical CO_2 concentrations is 35.3% (0–1 km), 36.2% (1–2 km), and 34.0% (2–3 km) in Shanghai, and 35.9% (0–1 km), 35.0% (1–2 km), and 32.9% (2–3 km) in YRD region. Conversely, the contribution of reduced power emission increases with height, accounting for 10.6% (0–1 km), 12.7% (1–2 km), and 14.3% (2–3 km) in Shanghai, and 11.4% (0–1 km), 13.7% (1–2 km), and 15.3% (2–3 km) in YRD region. For residential emission, its contribution

is 4.6% (0–1 km), 2.9% (1–2 km), and 9.7% (2–3 km) in Shanghai, 4.3% (0–1 km), 6.3% (1–2 km), and 8.7% (2–3 km).

4. Conclusions and Discussion

The unintentional emission reductions during the COVID-19 pandemic provides a unique opportunity to investigate the response of CO_2 concentrations to emission reductions and gain a better understanding of CO_2 sinks and sources over YRD region. In this study, WRF-VPRM model coupled with high-resolution dynamic emission inventory and surface observations were used to quantify the impact of emission reduction on spatiotemporal changes of CO_2 concentrations in YRD region during the COVID-19 pandemic. The model with dynamic emission shows a better agreement with surface observations than the other two emission inventory (ODIAC and EDGAR), providing confidence in the quantification of CO_2 concentrations variations. Model results show that prominent reduction in CO_2 concentrations due to emission reduction is concentrated along the Yangtze River and Hangzhou Bay, where industrial and transportation emissions are most densely distributed. Emission reductions lead to a CO_2 decrease of 4.6 ppmv (−1.1%) in Shanghai and 3.1 ppmv (−0.7%) in YRD region, while meteorological conditions have a negligible impact in Shanghai (−0.17 ppmv, −0.04%) and cause a 0.66 ppmv (0.15%) increase in YRD region. For XCO_2, emission reductions contribute to a 0.20 ppmv (−0.05%) decrease in Shanghai and a −0.15 ppmv (−0.04%) in YRD region, while meteorology variations contribute to a −0.07 ppmv (−0.02%) in Shanghai and 0.03 ppmv (0.01%) in YRD region, respectively.

Furthermore, a series of model experiments reveal that transportation and industrial emissions reductions are major contributors for the decline in near-surface CO_2 concentration, accounting for 45.8% (42.6%) and 34.9% (47%) in Shanghai (YRD). In addition, CO_2 concentrations respond quickly to reduced transportation emission during the initial lockdown period, and then the contributions of industrial and power emissions to CO_2 reduction gradually increase in both Shanghai and YRD region. The impact of power emission on CO_2 concentrations is relatively smaller at the surface and it becomes distinct as altitude increases. Residential emission has a minor impact to decline in CO_2 concentrations, and produces positive impact in Anhui Province due to a small increase in residential heating in winter. Our findings contribute to a better understanding of dynamic CO_2 variations and the response of CO_2 concentrations to emission reductions, which is helpful for emission management and climate adaption policies.

Nevertheless, even after dynamic emission is used in WRF-VPRM, simulated CO_2 variations are still having biases comparing with the surface observations. We noticed that CO_2 concentrations are overestimated by 2.5 ppmv at Dongtan using dynamic emission (Table 3). This overestimation happens more often at midnight in rural areas where anthropogenic sources are less of a factor. It could be related to the uncertainty of the initial and boundary conditions and stable boundary layer structure (Hu et al., 2013, 2021a). In addition to this factor, there are a few other factors that may introduce the model biases, including the uncertainties in the parameterization of terrestrial respiration, VPRM parameters and simulated meteorological fields. X. Li et al. (2020) pointed out the uncertainty of terrestrial CO_2 fluxes largely depends on VPRM parameters, especially maximum light use efficiency. More CO_2 fluxes observations are urgently needed to optimize VPRM parameters in China (Kountouris et al., 2018). Previous studies demonstrated that regional transport can significantly impact CO_2 concentrations. Weather system, such as cold front (Hu et al., 2020), can modulate CO_2 gradients across fronts. A mischaracterized wind filed therefore could lead to model biases and therefore accurate meteorological condition is also crucial for CO_2 simulations. In summary, efforts are still needed to improve CO_2 simulations, and accurate modeling is a basis for inverse estimates of CO_2 flux in the next step.

Data Availability Statement

All simulation results, CO_2 surface observations data from Lin'an, Zhangjiang and Dongtan, as well as meteorological data for validation can be obtained from Y. Wang (2023). The Open-source Data Inventory for Anthropogenic CO_2 (ODIAC) emission data (Oda & Maksyutov, 2015) and EDGAR emission data (Crippa et al., 2022b) were used in this study. The mole fraction product of CO_2 for initial and boundary condition and for validation were provided by ECMWF Copernicus Atmosphere Monitoring Service (CAMS) (CAMS, 2020). CO_2 aircraft observations were provide by CONTRAIL (Comprehensive Observation Network for Trace gases by

Airliner) Program (Machida et al., 2018). Figures were made with Matplotlib version 3.5.2 (Caswell et al., 2022; Hunter, 2007), available under the Matplotlib license at https://matplotlib.org/.

References

Agustí-Panareda, A., Barré, J., Massart, S., Inness, A., Aben, I., Ades, M., et al. (2023). Technical note: The CAMS greenhouse gas reanalysis from 2003 to 2020. *Atmospheric Chemistry and Physics*, 23(6), 3829–3859. https://doi.org/10.5194/acp-23-3829-2023

Ahmadov, R., Gerbig, C., Kretschmer, R., Koerner, S., Neininger, B., Dolman, A. J., & Sarrat, C. (2007). Mesoscale covariance of transport and CO_2 fluxes: Evidence from observations and simulations using the WRF-VPRM coupled atmosphere-biosphere model. *Journal of Geophysical Research*, 112(D22), D22107. https://doi.org/10.1029/2007JD008552

An, J., Huang, Y., Huang, C., Wang, X., Yan, R., Wang, Q., et al. (2021). Emission inventory of air pollutants and chemical speciation for specific anthropogenic sources based on local measurements in the Yangtze River Delta region, China. *Atmospheric Chemistry and Physics*, 21(3), 2003–2025. https://doi.org/10.5194/acp-21-2003-2021

Buchwitz, M., Reuter, M., Noel, S., Bramstedt, K., Schneising, O., Hilker, M., et al. (2021). Can a regional-scale reduction of atmospheric CO_2 during the COVID-19 pandemic be detected from space? A case study for east China using satellite XCO_2 retrievals. *Atmospheric Measurement Techniques*, 14(3), 2141–2166. https://doi.org/10.5194/amt-14-2141-2021

Caswell, T., Droettboom, M., Lee, A., Hunter, J., Firing, E., Stansby, D., et al. (2022). Matplotlib v3.5.2 [Software]. Zenodo. https://doi.org/10.5281/zenodo.6513224

Che, K., Cai, Z. N., Liu, Y., Wu, L., Yang, D. X., Chen, Y. C., et al. (2022). Lagrangian inversion of anthropogenic CO_2 emissions from Beijing using differential column measurements. *Environmental Research Letters*, 17(7), 075001. https://doi.org/10.1088/1748-9326/ac7477

Chen, F., & Dudhia, J. (2001). Coupling an advanced land surface-hydrology model with the Penn State-NCAR MM5 modeling system. Part I: Model implementation and sensitivity. *Monthly Weather Review*, 129(4), 569–585. https://doi.org/10.1175/1520-0493(2001)129<0569:CAALSH>2.0.CO;2

Chevallier, F., Zheng, B., Broquet, G., Ciais, P., Liu, Z., Davis, S. J., et al. (2020). Local anomalies in the column-averaged dry air mole fractions of carbon dioxide across the globe during the first months of the coronavirus recession. *Geophysical Research Letters*, 47(22), e2020GL090244. https://doi.org/10.1029/2020GL090244

Copernicus Atmosphere Monitoring Service (CAMS). (2020). CAMS global inversion-optimised greenhouse gas fluxes and concentrations [Dataset]. Retrieved from https://ads.atmosphere.copernicus.eu/cdsapp#!/dataset/cams-global-greenhouse-gas-inversion?tab=overview

Crippa, M., Guizzardi, D., Banja, M., Solazzo, E., Muntean, M., Schaaf, E., et al. (2022a). *CO_2 emissions of all world countries*. JRC/IEA/PBL 2022 Report, EUR 31182 EN. Publications Office of the European Union. JRC130363. https://doi.org/10.2760/730164

Crippa, M., Guizzardi, D., Banja, M., Solazzo, E., Muntean, M., Schaaf, E., et al. (2022b). EDGAR emission dataset (EDGAR v7.0) [Dataset]. The Directorate-General for Joint Research Centre, European Commission. Retrieved from https://edgar.jrc.ec.europa.eu/dataset_ghg70

Dacre, H. F., Western, L. M., Say, D., O'Doherty, S., Arnold, T., Rennick, C., & Hawkins, E. (2021). Detectability of COVID-19 global emissions reductions in local CO_2 concentration measurements. *Environmental Research Letters*, 16(9), 094043. https://doi.org/10.1088/1748-9326/acleda

Diao, Y., Huang, J., Liu, C., Cui, J., & Liu, S. (2015). A modeling study of CO_2 flux and concentrations over the Yangtze River Delta using the WRF-GHG model. *Chinese Journal of Atmospheric Sciences*, 39(5), 849–860. (In Chinese).

Dong, X., Yue, M., Jiang, Y., Hu, X.-M., Ma, Q., Pu, J., & Zhou, G. (2021). Analysis of CO_2 spatio-temporal variations in China using a weather-biosphere online coupled model. *Atmospheric Chemistry and Physics*, 21(9), 7217–7233. https://doi.org/10.5194/acp-21-7217-2021

Dudhia, J. (1989). Numerical study of convection observed during the winter monsoon experiment using a mesoscale two-dimensional model. *Journal of the Atmospheric Sciences*, 46(20), 3077–3107. https://doi.org/10.1175/1520-0469(1989)046<3077:NSOCOD>2.0.CO;2

Eldering, A., Wennberg, P. O., Crisp, D., Schimel, D. S., Gunson, M. R., Chatterjee, A., et al. (2017). The Orbiting Carbon Observatory-2 early science investigations of regional carbon dioxide fluxes. *Science*, 358(6360), eaam5745. https://doi.org/10.1126/science.aam5745

Esteki, K., Prakash, N., Li, Y., Mu, C., & Du, K. (2017). Seasonal variation of CO_2 vertical distribution in the atmospheric boundary layer and impact of meteorological parameters. *International Journal of Environmental Research*, 11(5–6), 707–721. https://doi.org/10.1007/s41742-017-0062-y

Feng, S., Lauvaux, T., Newman, S., Rao, P., Ahmadov, R., Deng, A., et al. (2016). Los Angeles megacity: A high-resolution land-atmosphere modelling system for urban CO_2 emissions. *Atmospheric Chemistry and Physics*, 16(14), 9019–9045. https://doi.org/10.5194/acp-16-9019-2016

Feng, T., Zhou, W., Wu, S., Niu, Z., Cheng, P., Xiong, X., & Li, G. (2019). High-resolution simulation of wintertime fossil fuel CO_2 in Beijing, China: Characteristics, sources, and regional transport. *Atmospheric Environment*, 198, 226–235. https://doi.org/10.1016/j.atmosenv.2018.10.054

Friedl, M. A., McIver, D. K., Hodges, J. C. F., Zhang, X. Y., Muchoney, D., Strahler, A. H., et al. (2002). Global land cover mapping from MODIS: Algorithms and early results. *Remote Sensing of Environment*, 83(1–2), 287–302. https://doi.org/10.1016/S0034-4257(02)00078-0

Gourdji, S., Karion, A., Lopez-Coto, I., Ghosh, S., Whetstone, J., Zhou, Y., et al. (2022). A modified Vegetation Photosynthesis and Respiration Model (VPRM) for the eastern USA and Canada, evaluated with comparison to atmospheric observations and other biospheric models. *Journal of Geophysical Research: Biogeosciences*, 127, e2021JG006290. https://doi.org/10.1029/2021JG006290

Grell, G. A., & Devenyi, D. (2002). A generalized approach to parameterizing convection combining ensemble and data assimilation techniques. *Geophysical Research Letters*, 29(14), 38-1–38-4. https://doi.org/10.1029/2002GL015311

Han, P. F., Zeng, N., Oda, T., Lin, X. H., Crippa, M., Guan, D. B., et al. (2020). Evaluating China's fossil-fuel CO_2 emissions from a comprehensive dataset of nine inventories. *Atmospheric Chemistry and Physics*, 20(19), 11371–11385. https://doi.org/10.5194/acp-20-11371-2020

Hong, S.-Y., Noh, Y., & Dudhia, J. (2006). A new vertical diffusion package with an explicit treatment of entrainment processes. *Monthly Weather Review*, 134(9), 2318–2341. https://doi.org/10.1175/MWR3199.1

Hu, X.-M., Crowell, S., Wang, Q., Zhang, Y., Davis, K. J., Xue, M., et al. (2020). Dynamical downscaling of CO_2 in 2016 over the contiguous United States using WRF-VPRM, a Weather-Biosphere-Online-Coupled Model. *Journal of Advances in Modeling Earth Systems*, 12(4), e2019MS001875. https://doi.org/10.1029/2019MS001875

Hu, X.-M., Gourdji, S. M., Davis, K. J., Wang, Q., Zhang, Y., Xue, M., et al. (2021a). Implementation of improved parameterization of terrestrial flux in WRF-VPRM improves the simulation of nighttime CO_2 peaks and a daytime CO_2 band ahead of a cold front. *Journal of Geophysical Research: Atmospheres*, 126(10), e2020JD034362. https://doi.org/10.1029/2020JD034362

Hu, X.-M., Hu, J., Gao, L., Cai, C., Jiang, Y., Xue, M., et al. (2021b). Multisensor and multimodel monitoring and investigation of a wintertime air pollution event ahead of a cold front over eastern China. *Journal of Geophysical Research: Atmospheres*, 126(10), e2020JD033538. https://doi.org/10.1029/2020JD033538

Hu, X.-M., Klein, P. M., & Xue, M. (2013). Evaluation of the updated YSU Planetary Boundary Layer Scheme within WRF for Wind Resource and Air Quality Assessments. *Journal of Geophysical Research: Atmospheres*, *118*, 10490–10505. https://doi.org/10.1002/jgrd.50823

Hu, X.-M., Xue, M., & McPherson, R. A. (2017). The importance of soil-type contrast in modulating August precipitation distribution near the Edwards Plateau and Balcones Escarpment in Texas. *Journal of Geophysical Research: Atmospheres*, *122*(20), 10711–10728. https://doi.org/10.1002/2017JD027035

Hu, X.-M., Xue, M., McPherson, R. A., Martin, E., Rosendahl, D. H., & Qiao, L. (2018). Precipitation dynamical downscaling over the Great Plains. *Journal of Advances in Modeling Earth Systems*, *10*(2), 421–447. https://doi.org/10.1002/2017MS001154

Huang, C., An, J., Wang, H., Liu, Q., Tian, J., Wang, Q., et al. (2021). Highly resolved dynamic emissions of air pollutants and greenhouse gas CO_2 during COVID-19 pandemic in east China. *Environmental Science & Technology Letters*, *8*(10), 853–860. https://doi.org/10.1021/acs.estlett.1c00600

Hunter, J. D. (2007). Matplotlib: A 2D graphics environment. *Computing in Science & Engineering*, *9*(3), 90–95. https://doi.org/10.1109/MCSE.2007.55

Intergovernmental Panel on Climate Change (IPCC). (2007). *Climate change 2007: The physical science basis* (p. 996). Cambridge University Press.

IPCC. (2018). Global warming of 1.5°C. An IPCC special report on the impacts of global warming of 1.5°C above pre-industrial levels and related global greenhouse gas emission pathways, in the context of strengthening the global response to the threat of climate change, sustainable development, and efforts to eradicate poverty. Retrieved from https://www.ipcc.ch/sr15/

Keeling, C. D., Chin, J. F. S., & Whorf, T. P. (1996). Increased activity of northern vegetation inferred from atmospheric CO_2 measurements. *Nature*, *382*(6587), 146–149. https://doi.org/10.1038/382146a0

Kountouris, P., Gerbig, C., Rödenbeck, C., Karstens, U., Koch, T. F., & Heimann, M. (2018). Atmospheric CO_2 inversions on the mesoscale using data-driven prior uncertainties: Quantification of the European terrestrial CO_2 fluxes. *Atmospheric Chemistry and Physics*, *18*(4), 3047–3064. https://doi.org/10.5194/acp-18-3047-2018

Kretschmer, R., Gerbig, C., Karstens, U., & Koch, F.-T. (2012). Error characterization of CO_2 vertical mixing in the atmospheric transport model WRF-VPRM. *Atmospheric Chemistry and Physics*, *12*(5), 2441–2458. https://doi.org/10.5194/acp-12-2441-2012

Le Quéré, C., Jackson, R. B., Jones, M. W., Smith, A. J. P., Abernethy, S., Andrew, R. M., et al. (2020). Temporary reduction in daily global CO_2 emissions during the COVID-19 forced confinement. *Nature Climate Change*, *10*(7), 647–653. https://doi.org/10.1038/s41558-020-0797-x

Li, X., Hu, X.-M., Cai, C., Jia, Q., Zhang, Y., Liu, J., et al. (2020). Terrestrial CO_2 fluxes, concentrations, sources and budget in northeast China: Observational and modeling studies. *Journal of Geophysical Research: Atmospheres*, *125*(6), e2019JD031686. https://doi.org/10.1029/2019JD031686

Li, Y. L., Deng, J. J., Mu, C., Xing, Z. Y., & Du, K. (2014). Vertical distribution of CO_2 in the atmospheric boundary layer: Characteristics and impact of meteorological variables. *Atmospheric Environment*, *91*, 110–117. https://doi.org/10.1016/j.atmosenv.2014.03.067

Lian, J., Lauvaux, T., Utard, H., Bréon, F.-M., Broquet, G., Ramonet, M., et al. (2023). Can we use atmospheric CO_2 measurements to verify emission trends reported by cities? Lessons from a six-year atmospheric inversion over Paris. *EGUsphere* [preprint]. https://doi.org/10.5194/egusphere-2023-401

Liang, Z. T., Tang, W. H., Zeng, N., Cai, Q. X., Han, P. F., Zhang, Y., et al. (2022). Simulation of surface atmospheric CO_2 concentration in Beijing-Tianjin-Hebei region based on WRF model. *Transactions of Atmospheric Sciences*, *45*(3), 387–396. (In Chinese). https://doi.org/10.13878/j.cnki.dqkxxb.20220228018

Liu, C. (2015). Modeling study of CO_2 biosphere flux and concentration in Yangtze River Delta based on WRF-VPRM (Master's thesis). (In Chinese).

Liu, D., Sun, W., Zeng, N., Han, P., Yao, B., Liu, Z., et al. (2021). Observed decreases in on-road CO_2 concentrations in Beijing during COVID-19 restrictions. *Atmospheric Chemistry and Physics*, *21*(6), 4599–4614. https://doi.org/10.5194/acp-21-4599-2021

Liu, Z., Ciais, P., Deng, Z., Lei, R., Davis, S. J., Feng, S., et al. (2020). Near-real-time monitoring of global CO_2 emissions reveals the effects of the COVID-19 pandemic. *Nature Communications*, *11*(1), 5172. https://doi.org/10.1038/s41467-020-18922-7

Machida, T., Ishijima, K., Niwa, Y., Tsuboi, K., Sawa, Y., Matsueda, H., & Sasakawa, M. (2018). Atmospheric CO_2 mole fraction data of CONTRAIL-CME [Dataset], ver. 2023.1.0. Center for Global Environmental Research, NIES. Retrieved from https://cger.nies.go.jp/contrail/about/index.htm

Machida, T., Matsueda, H., Sawa, Y., Nakagawa, Y., Hirotani, K., Kondo, N., et al. (2008). Worldwide measurements of atmospheric CO_2 and other trace gas species using commercial airlines. *Journal of Atmospheric and Oceanic Technology*, *25*(10), 1744–1754. https://doi.org/10.1175/2008JTECHA1082.1

Mahadevan, P., Wofsy, S. C., Matross, D. M., Xiao, X., Dunn, A. L., Lin, J. C., et al. (2008). A satellite-based biosphere parameterization for net ecosystem CO_2 exchange: Vegetation Photosynthesis and Respiration Model (VPRM). *Global Biogeochemical Cycles*, *22*(2), GB2005. https://doi.org/10.1029/2006GB002735

Mlawer, E. J., Taubman, S. J., Brown, P. D., Iacono, M. J., & Clough, S. A. (1997). Radiative transfer for inhomogeneous atmospheres: RRTM, a validated correlated-k model for the longwave. *Journal of Geophysical Research*, *102*(D14), 16663–16682. https://doi.org/10.1029/97JD00237

Monteiro, V., Miles, N. L., Richardson, S. J., Turnbull, J., Karion, A., Kim, J., et al. (2022). The impact of the COVID-19 lockdown on greenhouse gases: A multi-city analysis of in situ atmospheric observations. *Environmental Research Communications*, *4*(4), 041004. https://doi.org/10.1088/2515-7620/ac66cb

Oda, T., Bun, R., Kinakh, V., Topylko, P., Halushchak, M., Marland, G., et al. (2019). Errors and uncertainties in a gridded carbon dioxide emissions inventory. *Mitigation and Adaptation Strategies for Global Change*, *24*(6), 1007–1050. https://doi.org/10.1007/s11027-019-09877-2

Oda, T., & Maksyutov, S. (2015). ODIAC fossil fuel CO_2 emissions dataset (ODIAC2022) [Dataset]. Center for Global Environmental Research, National Institute for Environmental Studies. https://doi.org/10.17595/20170411.001

Oda, T., Maksyutov, S., & Andres, R. J. (2018). The Open-source Data Inventory for Anthropogenic CO_2, version 2016 (ODIAC2016): A global monthly fossil fuel CO_2 gridded emissions data product for tracer transport simulations and surface flux inversions. *Earth System Science Data*, *10*(1), 87–107. https://doi.org/10.5194/essd-10-87-2018

Park, C., Gerbig, C., Newman, S., Ahmadov, R., Feng, S., Gurney, K. R., et al. (2018). CO_2 transport, variability, and budget over the southern California air basin using the high-resolution WRF-VPRM model during the CalNex 2010 Campaign. *Journal of Applied Meteorology and Climatology*, *57*(6), 1337–1352. https://doi.org/10.1175/jamc-d-17-0358.1

Park, C., Park, S. Y., Gurney, K. R., Gerbig, C., DiGangi, J. P., Choi, Y., & Lee, H. W. (2020). Numerical simulation of atmospheric CO_2 concentration and flux over the Korean Peninsula using WRF-VPRM model during Korus-AQ 2016 campaign. *PLoS One*, *15*(1), e0228106. https://doi.org/10.1371/journal.pone.0228106

Pillai, D., Gerbig, C., Ahmadov, R., Roedenbeck, C., Kretschmer, R., Koch, T., et al. (2011). High-resolution simulations of atmospheric CO_2 over complex terrain - Representing the Ochsenkopf mountain tall tower. *Atmospheric Chemistry and Physics*, *11*(15), 7445–7464. https://doi.org/10.5194/acp-11-7445-2011

Pillai, D., Gerbig, C., Marshall, J., Ahmadov, R., Kretschmer, R., Koch, T., & Karstens, U. (2010). High resolution modeling of CO_2 over Europe: Implications for representation errors of satellite retrievals. *Atmospheric Chemistry and Physics*, *10*(1), 83–94. https://doi.org/10.5194/acp-10-83-2010

Pu, J.-J., Hu, H. H., Jiang, Y. J., Du, R. G., & Qi, B. (2018). Characteristics of and factors affecting atmospheric CO_2 concentration in Hangzhou. *Environmental Science*, *39*, 3082–3089. (In Chinese). https://doi.org/10.13227/j.hjkx.201708258

Pu, J.-J., Xu, H.-H., He, J., Fang, S.-X., & Zhou, L.-X. (2014). Estimation of regional background concentration of CO_2 at Lin'an Station in Yangtze River Delta, China. *Atmospheric Environment*, *94*, 402–408. https://doi.org/10.1016/j.atmosenv.2014.05.060

Schwandner, F. M., Gunson, M. R., Miller, C. E., Carn, S. A., Eldering, A., Krings, T., et al. (2017). Spaceborne detection of localized carbon dioxide sources. *Science*, *358*(6360), eaam5782. https://doi.org/10.1126/science.aam5782

Sim, S., Lee, H., Oh, E., Kim, S., Ciais, P., Piao, S., et al. (2022). Short-term reduction of regional enhancement of atmospheric CO_2 in China during the first COVID-19 pandemic period. *Environmental Research Letters*, *17*(2), 024036. https://doi.org/10.1088/1748-9326/ac507d

Takahashi, T., Sutherland, S. C., Wanninkhof, R., Sweeney, C., Feely, R. A., Chipman, D. W., et al. (2009). Climatological mean and decadal change in surface ocean pCO(2), and net sea-air CO_2 flux over the global oceans. *Deep-Sea Research Part II: Topical Studies in Oceanography*, *56*(8–10), 554–577. https://doi.org/10.1016/j.dsr2.2008.12.009

Turner, A. J., Kim, J., Fitzmaurice, H., Newman, C., Worthington, K., Chan, K., et al. (2020). Observed impacts of COVID-19 on urban CO_2 emissions. *Geophysical Research Letters*, *47*(22), e2020GL090037. https://doi.org/10.1029/2020GL090037

Venturi, S., Randazzo, A., Tassi, F., Gioli, B., Bucciantti, A., Gualtieri, G., et al. (2021). Unveiling the changes in urban atmospheric CO_2 in the time of COVID-19 pandemic: A case study of Florence (Italy). *Science of the Total Environment*, *795*, 148877. https://doi.org/10.1016/j.scitotenv.2021.148877

Wang, H., Huang, C., Tao, W., Gao, Y., Wang, S., Jing, S., et al. (2022). Seasonality and reduced nitric oxide titration dominated ozone increase during COVID-19 lockdown in eastern China. *Npj Climate and Atmospheric Science*, *5*(1), 24. https://doi.org/10.1038/s41612-022-00249-3

Wang, W., Tian, Y., Liu, C., Sun, Y., Liu, W., Xie, P., et al. (2017). Investigating the performance of a greenhouse gas observatory in Hefei, China. *Atmospheric Measurement Techniques*, *10*(7), 2627–2643. https://doi.org/10.5194/amt-10-2627-2017

Wang, X., & Zhang, R. (2020). How did air pollution change during the COVID-19 outbreak in China? *Bulletin of the American Meteorological Society*, *101*(10), E1645–E1652. https://doi.org/10.1175/BAMS-D-20-0102.1

Wang, Y. (2023). Data related to CO_2 simulation [Dataset]. Zenodo. https://doi.org/10.5281/zenodo.8111919

Wei, C., Wang, M., Fu, Q., Dai, C., Huang, R., & Bao, Q. (2020). Temporal characteristics of greenhouse gases (CO_2 and CH_4) in the megacity Shanghai, China: Association with air pollutants and meteorological conditions. *Atmospheric Research*, *235*, 104759. https://doi.org/10.1016/j.atmosres.2019.104759

Wu, S., Zhou, W., Xiong, X., Burr, G. S., Cheng, P., Wang, P., et al. (2021). The impact of COVID-19 lockdown on atmospheric CO_2 in Xi'an, China. *Environmental Research*, *197*, 111208. https://doi.org/10.1016/j.envres.2021.111208

Xie, F., Lin, Y.-C., Ren, L., Gul, C., Wang, J.-Q., Cao, F., et al. (2022). Decrease of atmospheric black carbon and CO_2 concentrations due to COVID-19 lockdown at the Mt. Waliguan WMO/GAW baseline station in China. *Environmental Research*, *211*, 112984. https://doi.org/10.1016/j.envres.2022.112984

Yadav, V., Ghosh, S., Mueller, K., Karion, A., Roest, G., Gourdji, S. M., et al. (2021). The impact of COVID-19 on CO_2 emissions in the Los Angeles and Washington DC/Baltimore Metropolitan Areas. *Geophysical Research Letters*, *48*(11), e2021GL092744. https://doi.org/10.1029/2021GL092744

Zeng, N., Han, P., Liu, Z., Liu, D., Oda, T., Martin, C., et al. (2022). Global to local impacts on atmospheric CO_2 from the COVID-19 lockdown, biosphere and weather variabilities. *Environmental Research Letters*, *17*(1), 015003. https://doi.org/10.1088/1748-9326/ac3f62

Zheng, B., Geng, G., Ciais, P., Davis, S. J., Martin, R., Meng, J., et al. (2020). Satellite-based estimates of decline and rebound in China's CO_2 emissions during COVID-19 pandemic. *Science Advances*, *6*(49), eabd4998. https://doi.org/10.1126/sciadv.abd4998